




Partial Freezing for MIMO Adaptive Equalizers: Precise Demodulation in Dynamic Environments

Akira Kawai , *Member, IEEE*, Masanori Nakamura , *Member, IEEE*, Minami Takahashi, Takayuki Kobayashi , *Member, IEEE*, and Yutaka Miyamoto, *Member, IEEE*

Abstract—We propose partially frozen (PF) multiple-input multiple-output (MIMO) adaptive equalizers (AEQs). By increasing the degrees of freedom (DOFs) of widely used complex 2×2 MIMO AEQs, complex 4×2 and 8×2 MIMO AEQs can cope with various signal impairments that occur within a transmitter and receiver, such as in-phase/quadrature (IQ) skew and IQ imbalance. Although precise signal demodulation with such MIMO AEQs are useful for enhancing the information rate of a transmission even to reach beyond 1 Tb/s, the increase in internal DOFs ultimately comes with a decrease in the speed of tracking polarization fluctuations and an increase in computational complexity, which are problematic for efficient demodulation in a dynamic environment. To solve this, as the speed of fluctuation in the state of polarization (SOP) of the signal is much faster than those of impairments within the transmitter and receiver, PF MIMO AEQs reduce effective DOFs by separating each DOF corresponding to the SOP, transmitter, and receiver, then freezing unnecessary updates of transmitter and receiver DOFs. In this article, we describe the principle and show the results of numerical simulations and experiments with 128-Gbaud quadrature phase shift keying (QPSK) signals under IQ impairments. PF MIMO AEQs increased the tracking speed of the 8×2 MIMO AEQ, enabling the tracking of polarization fluctuations of over 11 Mrad/s (faster than fluctuation induced by lightning strikes) with less computational complexity than the conventional configuration. This method is a promising solution for high-speed data transmissions in dynamic environments.

Index Terms—Adaptive equalizers, digital signal processing, optical fiber communication.

I. INTRODUCTION

A MULTIPLE-INPUT multiple-output (MIMO) adaptive equalizer (AEQ) is a key technology used in digital coherent systems [1]. Digital signal processing (DSP)-based techniques, especially complex 2×2 MIMO AEQs that use two polarization components as input and output, have enabled adaptive compensation for dynamic polarization-related signal impairments, such as changes in the state of polarization (SOP) of a signal, polarization mode dispersion (PMD), and polarization dependent loss (PDL), which once were main limiting

factors of long-haul transmission. Since they have a greater impact on the signal with a broader bandwidth and higher-order modulation format, MIMO AEQs continue to be important even in high-information-rate optical transmitters and receivers with a net data rate of over 1 Tb/s [1].

As digital coherent systems have developed, it has been found that MIMO AEQs can compensate for electrical signal in-phase/quadrature (IQ) impairments in the transmitter and receiver, alongside those caused by polarization-related effects in the transmission line, by increasing their internal degrees of freedom (DOFs) [1], [2], [3], [4], [5]. Here, IQ impairments refer to IQ skew, IQ imbalance (including those caused by electrical signal reflection) and IQ crosstalk, which reportedly can be limiting factors of high-information-rate transmissions [1], [2], [3], [4], [5], [6]. Typical examples of such AEQs are complex 4×2 MIMO AEQs (or widely linear AEQ) [2] and 8×2 MIMO AEQs [1]. Under chromatic dispersion (CD) of fiber transmission lines, the former can compensate for signal IQ impairments at the receiver, while the latter can compensate simultaneously at the transmitter and receiver. Although the IQ impairments can be measured prior to field installation and calibrated with a static digital filter in the transmitter and receiver [7], it is useful to deal with them adaptively since the IQ impairments change over time, albeit at a slow rate, due to aging and temperature changes of the transmitter and receiver.

However, the increase in the DOFs of MIMO AEQs has drawbacks of decreased tracking speed for dynamic fluctuation of SOPs and increased computational complexity. The tracking speed depends on the dimensionality of the input signals, which is equivalent to the number of DOFs within the MIMO AEQ. Large signal dimensionality causes increased lag-induced excess errors of adaptive filtering [8]. In addition, the tracking speed of the AEQ depends on a step size of update algorithms, e.g., decision-directed least mean square or constant modulus algorithms [9]. Since the maximum step size for the stable operation of a MIMO AEQ is bounded by the inverse of the input signal's covariance matrix' trace [8], large signal dimensionality results in reduced maximum step sizes, and the maximum tracking speed is slowed accordingly. These would reduce the tolerance to rapid SOP fluctuation such as electromagnetic disturbances due to lightning strikes (reported maximum fluctuation speed is over 5 [10] or 8 [11] Mrad/s). Computational complexity increases almost proportional to DOFs and causes additional DSP power consumption, although techniques such as frequency-domain

Manuscript received 15 November 2022; revised 1 February 2023; accepted 24 February 2023. Date of publication 3 March 2023; date of current version 9 June 2023. (Corresponding author: Akira Kawai.)

The authors are with the NTT Network Innovation Laboratories, NTT Corporation, Yokosuka 239-0847, Japan (e-mail: akira.kawai.ku@hco.ntt.co.jp; masanori.nakamura.cu@hco.ntt.co.jp; minami.takahashi.xr@hco.ntt.co.jp; takayuki.kobayashi.wt@hco.ntt.co.jp; yutaka.miyamoto.fb@hco.ntt.co.jp).

Color versions of one or more figures in this article are available at <https://doi.org/10.1109/JLT.2023.3251996>.

Digital Object Identifier 10.1109/JLT.2023.3251996

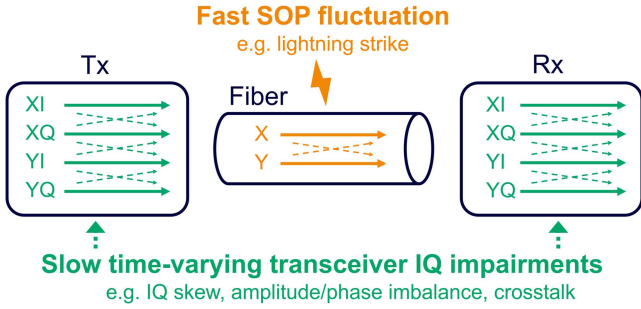


Fig. 1. Potential performance limiting factors of PDM transmission.

(FD) equalization [12], [13], [14] can be used to alleviate the complexity. These downsides could narrow the practical range of AEQs with increased DOFs.

In this work, we propose partially frozen (PF) MIMO AEQs as an extension of our previous work [15]. As shown in a previous study [16], one can separately estimate the characteristics of the transmitter and receiver IQ impairments from the coefficients of the MIMO AEQs with increased DOFs. Consequently, we can convert such DOFs to an equivalent cascade of smaller digital finite impulse response filters, each of which independently compensates for impairments regarding the SOP, transmitter, and receiver. The rate of characteristic change of DOFs with respect to the transmitter and receiver is much slower than that of the SOP, as shown in Fig. 1. Therefore, the transmitter- and receiver-related filter DOF updates can be temporarily frozen, and the transmission line-related DOF updates can continue. Since we can restart the update anytime, this PF MIMO AEQ can reduce the computational complexity and improve the filter tracking speed, without sacrificing adaptation ability to time-varying impairments within the transmitter and receiver. We discussed the computational complexity and showed the effectiveness of PF MIMO AEQs by simulation, and then presented the results of experiments using a 128-Gbaud signal. The experimental results showed that the PF MIMO AEQs of an 8×2 MIMO AEQ improved the polarization tracking speed by almost double, demonstrating the effectiveness of the PF MIMO AEQs for designing high-performance DSPs.

II. PRINCIPLE

A schematic representation of PF MIMO AEQs is shown in Fig. 2. PF MIMO AEQs are implemented in the receiver-side DSP. In this work, we define the output signal of the transmission line (or the input of the DSP) by a four-dimensional complex vector $\mathbf{s}_{out} = (s_{x,out}(\omega) s_{x,out}^*(-\omega) s_{y,out}(\omega) s_{y,out}^*(-\omega))^T$, where asterisks mean complex conjugate, because IQ impairments are equivalent to the frequency-dependent complex imbalance/crosstalk between the signal and its complex conjugate. Also, we define the demodulated input signal of the transmission line (or the output of the DSP) by a two-dimensional complex vector $\mathbf{s}_{in} = (s_{x,in}(\omega) s_{y,in}(\omega))^T$. Note that we use a different definition of the DSP input vector from those in previous studies [1], [2], [13], where inputs

are $(Re(s_{x,out}) Im(s_{x,out}) Re(s_{y,out}) Im(s_{y,out}))^T$ for convenience of mathematical description, although the two definitions are equivalent. Also, we assumed FD equalization [12], [13], [14] because it can reduce the computational complexity for large filter sizes and simplify the cascaded filtering operations described in the following.

First, we explain PF 8×2 MIMO AEQ, since 4×2 MIMO AEQs are almost same as the 8×2 MIMO AEQ except for an absence of a correction term for transmitter-side IQ impairments. CD of the signals is first compensated for. Next, signal impairments are compensated for with the MIMO AEQ except for a frequency offset of a local oscillator (LO). In the conventional 8×2 MIMO AEQ, this operation is essentially equal to computing products of two adaptively updatable 4×2 matrices and signal vectors, one of which is flipped with respect to the frequency and complex-conjugated (“Flip and conjugate” in the figure), in the FD. We define the adaptive matrix in a conventional 8×2 MIMO AEQ using $H_{8 \times 2,1}(\omega)$, $H_{8 \times 2,2}(\omega)$, and P that satisfy

$$H_{8 \times 2,1}(\omega) = \begin{pmatrix} h_{xxo,1}(\omega) & h_{xxc,1}(\omega) & h_{xyo,1}(\omega) & h_{xyc,1}(\omega) \\ h_{yxo,1}(\omega) & h_{yxc,1}(\omega) & h_{yyo,1}(\omega) & h_{yyc,1}(\omega) \end{pmatrix} \quad (1)$$

$$H_{8 \times 2,2}(\omega) = \begin{pmatrix} h_{xxo,2}(\omega) & h_{xxc,2}(\omega) & h_{xyo,2}(\omega) & h_{xyc,2}(\omega) \\ h_{yxo,2}(\omega) & h_{yxc,2}(\omega) & h_{yyo,2}(\omega) & h_{yyc,2}(\omega) \end{pmatrix} \quad (2)$$

and

$$P = \begin{pmatrix} 0 & 1 & 0 & 0 \\ 1 & 0 & 0 & 0 \\ 0 & 0 & 0 & 1 \\ 0 & 0 & 1 & 0 \end{pmatrix} \quad (3)$$

Finally, the carrier phase recovery (CPR) part then compensates for the effect of the frequency offset in the time domain.

The basic idea of the PF MIMO AEQ is based on transforming the MIMO AEQ part into a cascade of matrix multiplication operations as shown in the lower part of Fig. 2(a). A previous study [16] showed that 4 DOFs are sufficient to express each frequency component of transmitter/receiver IQ impairments, and one can obtain frequency characteristics of IQ impairments of a transmitter and receiver from the components of $H_{8 \times 2,1}$, $H_{8 \times 2,2}$. Using these findings, we can decompose $H_{8 \times 2,1}$, $H_{8 \times 2,2}$ as

$$H_{8 \times 2,1}(\omega) = H'_{SOP}(\omega) H'_R(\omega) \quad (4)$$

$$H_{8 \times 2,2}(\omega) = H'^*_T(-\omega) H'^*_{SOP}(-\omega) H'^*_R(-\omega) P. \quad (5)$$

Here,

$$H'_{SOP}(\omega) = \begin{pmatrix} h_{xx}(\omega) & h_{xy}(\omega) \\ h_{yx}(\omega) & h_{yy}(\omega) \end{pmatrix} \quad (6)$$

is a matrix that represents an inversed characteristic of SOP-related effects, that is, a combination of frequency-dependent SOP rotations, PMD, and PDL. $H'_{SOP}(\omega)$ is equivalent to an

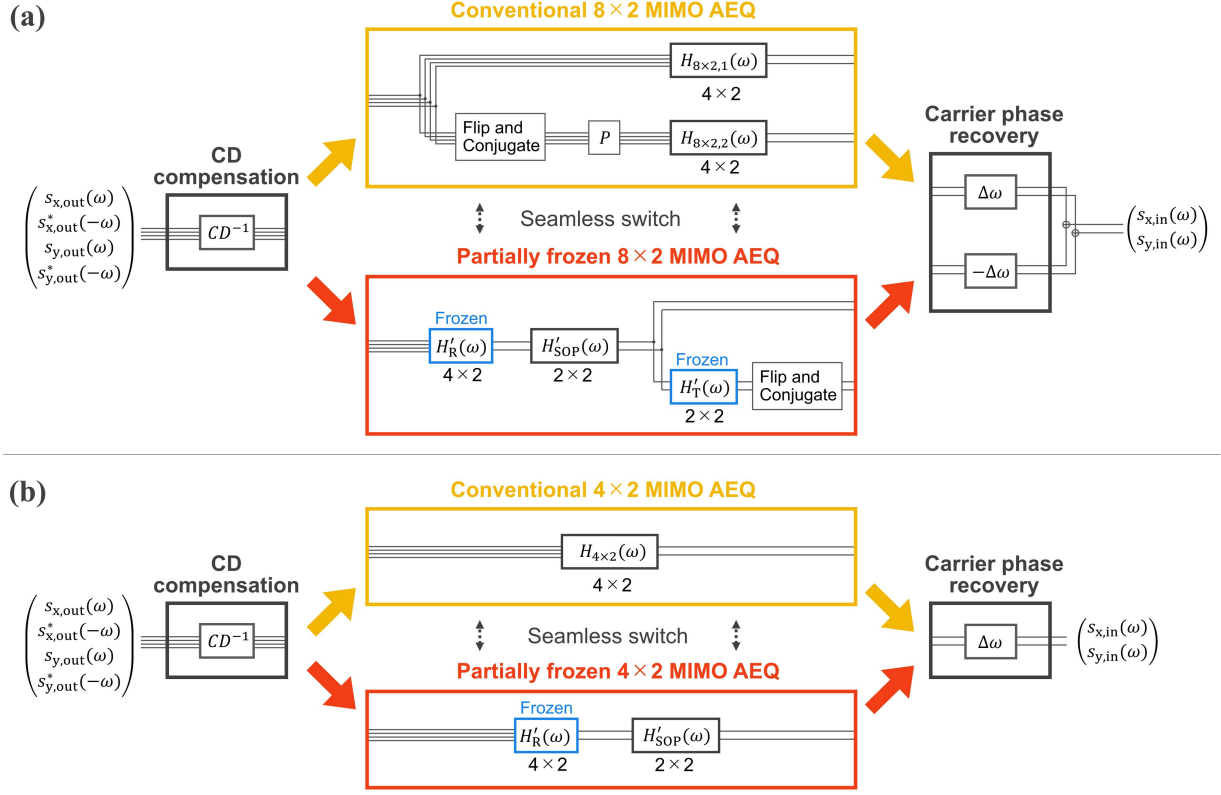


Fig. 2. Schematic representations of PF MIMO AEQs. (a) PF 8×2 MIMO AEQ. (b) PF 4×2 MIMO AEQ.

inversed Jones matrix of the entire transmission line. Also,

$$H'_R(\omega) = \begin{pmatrix} 1 & h_{R11}(\omega) & 0 & h_{R12}(\omega) \\ 0 & h_{R21}(\omega) & 1 & h_{R22}(\omega) \end{pmatrix} \quad (7)$$

is a matrix that represents the electrical IQ impairment characteristic of the receiver. Finally,

$$H'_T(\omega) = \begin{pmatrix} h_{T11}(\omega) & h_{T12}(\omega) \\ h_{T21}(\omega) & h_{T22}(\omega) \end{pmatrix} \quad (8)$$

is a matrix that represents the electrical IQ impairment characteristic of the transmitter. A derivation of the (4,5) is shown in Appendix A. Each component of the decomposed matrices can be expressed using the components of $H_{8 \times 2,1}$ and $H_{8 \times 2,2}$ as

$$\begin{pmatrix} h_{xx}(\omega) & h_{xy}(\omega) \\ h_{yx}(\omega) & h_{yy}(\omega) \end{pmatrix} = \begin{pmatrix} h_{x_{xo},1}(\omega) & h_{x_{yo},1}(\omega) \\ h_{y_{xo},1}(\omega) & h_{y_{yo},1}(\omega) \end{pmatrix} \quad (9)$$

$$\begin{pmatrix} h_{R11}(\omega) & h_{R12}(\omega) \\ h_{R21}(\omega) & h_{R22}(\omega) \end{pmatrix} = \begin{pmatrix} h_{x_{xo},1}(\omega) & h_{x_{yo},1}(\omega) \\ h_{y_{xo},1}(\omega) & h_{y_{yo},1}(\omega) \end{pmatrix}^{-1} \begin{pmatrix} h_{x_{xc},1}(\omega) & h_{x_{yc},1}(\omega) \\ h_{y_{xc},1}(\omega) & h_{y_{yc},1}(\omega) \end{pmatrix} \quad (10)$$

$$\begin{pmatrix} h_{T11}(\omega) & h_{T12}(\omega) \\ h_{T21}(\omega) & h_{T22}(\omega) \end{pmatrix} = \begin{pmatrix} h_{x_{xc},2}^*(-\omega) & h_{x_{yc},2}^*(-\omega) \\ h_{y_{xc},2}^*(-\omega) & h_{y_{yc},2}^*(-\omega) \end{pmatrix} \begin{pmatrix} h_{x_{xo},1}(\omega) & h_{x_{yo},1}(\omega) \\ h_{y_{xo},1}(\omega) & h_{y_{yo},1}(\omega) \end{pmatrix}^{-1} \quad (11)$$

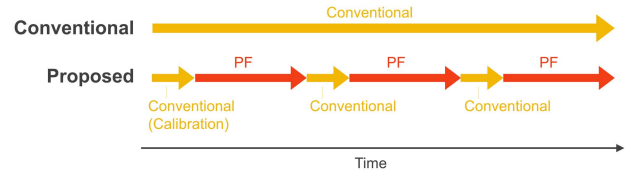


Fig. 3. Example of operation timeline of a PF MIMO AEQ.

as one can confirm from (4) and (5). Also, one can show from (5) that

$$\begin{pmatrix} h_{x_{xo},2}^*(-\omega) & h_{x_{yo},2}^*(-\omega) \\ h_{y_{xo},2}^*(-\omega) & h_{y_{yo},2}^*(-\omega) \end{pmatrix} = \begin{pmatrix} h_{R11}(\omega) & h_{R12}(\omega) \\ h_{R21}(\omega) & h_{R22}(\omega) \end{pmatrix} H'_{SOP}(\omega) H'_T(\omega) \quad (12)$$

holds.

These equations show the equivalence of filtering in the conventional and PF modes and ensure that we can seamlessly switch between the two modes and continue to compensate for the transmission impairments under CD. An example of the operation timeline of the PF MIMO AEQs is shown in Fig. 3. Here, we propose a fixed time-interval mode-changing operation as an example. Unlike the conventional operation where the AEQ is continuously operated in the conventional mode, the MIMO AEQ is switched to the PF mode after calibrating of $H'_T(\omega)$ and $H'_R(\omega)$ by the conventional mode. The MIMO

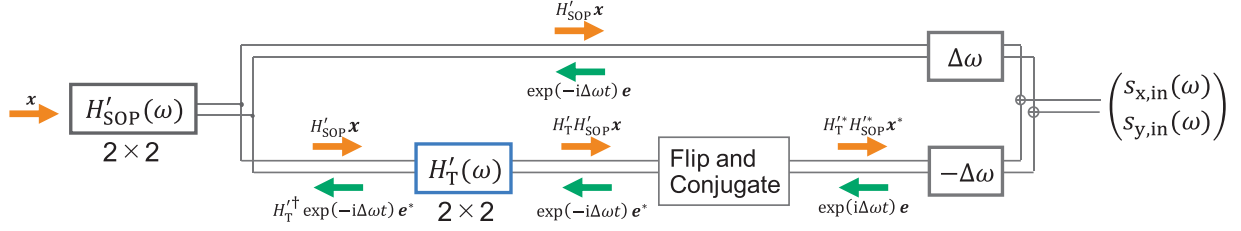


Fig. 4. Schematic of back propagation for updating H'_{SOP} .

AEQ switches back to the conventional mode at fixed time intervals and calibrate $H'_T(\omega)$ and $H'_R(\omega)$. It is also possible to adaptively change the mode by monitoring the SNR, BER, or constellation [17] of the demodulated signals. Note that the entire calibration process can be offloaded to external low-speed computing resources on which the conventional mode operation is implemented, to reduce the demand for high-speed real-time computing resources.

The PF 4×2 MIMO AEQ is also shown in Fig. 2(b). It is essentially same as the 8×2 MIMO AEQ except for the absence of $H'_T(\omega)$. To obtain $H'_R(\omega)$, (10) can also be used.

To update $H'_{SOP}(\omega)$ with low computational costs, the gradient decent approach is effective. For cascaded filters like PF MIMO AEQ, or more commonly known, deep neural networks, we can successively calculate the derivative of the demodulation error with respect to each filter (known as back propagation) from the output of the entire filter by the chain rule [4]. As shown in Fig. 4, we can obtain the update formula,

$$\begin{aligned} H'_{SOP}(m+1) &= H'_{SOP}(m) + \mu e \exp(-i\Delta\omega t) \mathbf{x}^\dagger \\ &\quad + \mu H'^\dagger_T(\omega) e^* \exp(-i\Delta\omega t) \mathbf{x}^\dagger \end{aligned} \quad (13)$$

where \dagger is a symbol of conjugate transpose, m is a time index, μ is a step size, e is an error vector that can be obtained by $e = s_{decision} - s_{in}$, and $\Delta\omega t$ is the phase factor backpropagated from the CPR part. Here, $s_{decision}$ is the demodulated signal after symbol decision. $s_{decision}$ can be substituted by pilot symbols. Also, $\mathbf{x} = H'_R(\omega)CD^{-1}s_{out}$ are input vector of H'_{SOP} . Additional computational costs are not required for a calculation of \mathbf{x} because it can be obtained in the process of forward filtering. To reduce the computational cost to calculate $H'_{SOP}(m+1)$, we can ignore the third term as

$$H'_{SOP}(m+1) = H'_{SOP}(m) + \mu e \exp(-i\Delta\omega t) \mathbf{x}^\dagger \quad (14)$$

since the third term (the correction term for transmitter IQ impairments) tends to be much smaller than the second term. For the update of H'_{SOP} in the PF 4×2 MIMO AEQ, (14) can be used without any approximation.

Required computational costs (the number of complex multiplications) for processing one fast Fourier transformation (FFT) block with each configuration of FD MIMO AEQs are summarized in Table I. Here, L is the length of the filter, which corresponds to the FFT size of the FD processing. The contribution of the FFT, CD compensation, complex additions, multiplication of

TABLE I
REQUIRED MULTIPLICATION NUMBER FOR MIMO AEQS

Type	Filtering	Updating	Total
2×2	4L	4L	8L
4×2	8L	8L	16L
8×2	16L	16L	32L
PF 4×2	8L	4L	12L
PF 8×2	12L	12L	24L
PF 8×2 (simple)	12L	4L	16L

the step size and CPR term are omitted from the estimation. Also, we considered the computational cost of matrix decomposition or multiplication associated with the mode-switching (9)–(12) to be negligible because the mode-switching requires much less frequency than the filtering and updating operation in Table I since the changes in the IQ impairment characteristics (which have a typical timescale of > 1 s) are much slower than the polarization fluctuation. Note that for the multiplication of $H'_R(\omega)$, the required multiplication is 4L because half of the components are 0 or 1. By switching to the PF mode, the multiplication number can be reduced to 3/4 for both the 8×2 and 4×2 MIMO AEQ. For the 8×2 MIMO AEQ, we can reduce it even more to half of the original number by adopting the simple update formula (14) instead of (13). These show PF MIMO AEQs can be more computationally cost effective than the conventional configurations.

To confirm the effectiveness of the PF configuration, we conducted numerical simulations. We emulated rapidly changing SOP by applying time variant SOP rotations represented by a Jones matrix J that satisfies

$$J = \begin{pmatrix} \cos \omega_0 t & -\sin \omega_0 t \\ \sin \omega_0 t & \cos \omega_0 t \end{pmatrix} \quad (15)$$

where ω_0 is angular frequency. We changed ω_0 from 0 to 11 Mrad/s. We also assumed other signal impairments; amplified spontaneous emission noise, frequency offset of the LO (100 MHz), phase noise (20 kHz), and IQ skews on both the transmitter and receiver (3 ps for both). We also added additive white Gaussian noise to the signal so that the signal-to-noise ratio (SNR) of the signal demodulated with the conventional 8×2 MIMO AEQ under no polarization fluctuation matched the experimental result (21.8 dB) shown in the next section. The signals were 128 Gbaud QPSK randomly generated by the Mersenne Twister with a frame length of 192000, and

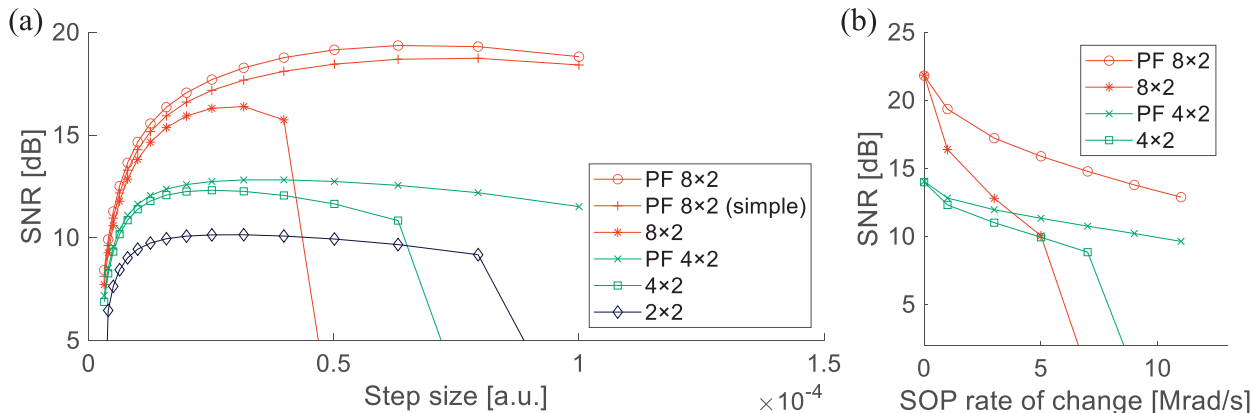


Fig. 5. Simulation results. (a) Relationship of step size and signal SNR after demodulation under SOP rotation under 1 Mrad/s. (b) Maximum demodulation performance with respect to the SOP rate of change.

demodulated by using 2 sample-per-symbol, 50% overlap-cut FD MIMO AEQs whose details are described in [13]. The FFT size of the MIMO AEQ was set at 1024. For the PF operation, we obtained H'_T and H'_R before the main measurement using five-frame signals. The CPR section consisted of coarse estimation with a 2nd-order digital phase-locked loop and fine estimation with a blind phase search algorithm [18]. The laser phase noise was compensated for in both the AEQ and CPR sections without explicit assignment. For the update in the PF 8×2 MIMO AEQ, both the original formula (13) and simplified formula (14) are implemented in a decision-directed way with periodically inserted pilot symbols (insertion rate: 0.016).

The results are shown in Fig. 5. We first changed the step size of the MIMO AEQs in 0.1-dB increments while fixing ω_0 at 1 Mrad/s. Generally, if the step size was too small, it could not follow the polarization rotation, and conversely, if it was too large, the convergence of the coefficients became unstable, resulting in a reduced SNR. As shown in Fig. 5(a), the PF configuration improved the SNR because of its low dimensionality, which leads to less lag-induced errors and larger maximum step sizes. The PF 8×2 MIMO AEQ performed better than the PF 4×2 MIMO AEQ since it can compensate not only for IQ skew in the receiver but also that in the transmitter. The use of the simple update formula (14) had little impact on the SNR with a maximum SNR difference of 0.7 dB. We then changed ω_0 and optimized the step size for each ω_0 . As shown in Fig. 5(b), although conventional MIMO AEQs rapidly failed as ω_0 increased, the PF MIMO AEQs succeeded in demodulating the signal with a rapid SOP rotation of 11 Mrad/s. Also, no significant SNR degradation between conventional and PF MIMO AEQs is observed with a 0 Mrad/s SOP rotation (quasi-stable channel).

From the linear interpolation of the results, we derived the SOP rate of change that causes a 1 dB SNR penalty. The results are summarized in Table II. It shows that the PF provides an improvement (almost double for the 8×2 MIMO AEQ) of the 1 dB tolerance.

TABLE II
SOP RATE OF CHANGE WITH A 1dB SNR PENALTY

Type	SOP rate of change with a 1dB SNR penalty [Mrad/s]
8×2	0.18
4×2	0.60
PF 8×2	0.41
PF 4×2	0.82

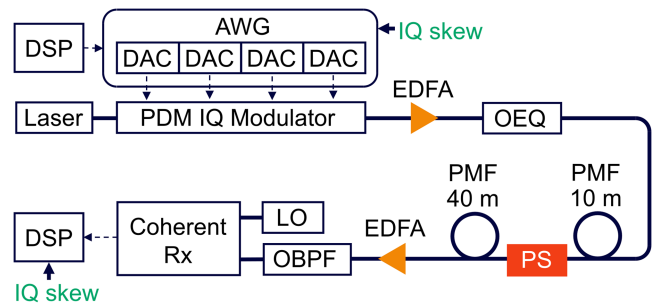


Fig. 6. Experimental setup.

III. EXPERIMENT

A. Experimental Setup

To test the feasibility of a PF MIMO AEQ in a realistic setup, we conducted a back-to-back signal generation and detection experiment, whose schematic illustration is shown in Fig. 6. We modulated monochromatic light at 193.755 THz from a narrow-linewidth laser. The modulation format was QPSK generated by the Mersenne Twister and the frame length was 65536. The signal was generated at 128 Gbaud and fed to an arbitrary waveform generator (AWG) that was operated at 128 Gsample/s with a bandwidth of 65 GHz. The electrical signals generated by the AWG drove a 35-GHz lithium-niobate-based polarization-division-multiplexed (PDM) IQ modulator. Wavelength selective switch-based optical equalization (OEQ) was conducted to roughly equalize the frequency response of the transmitter [19].

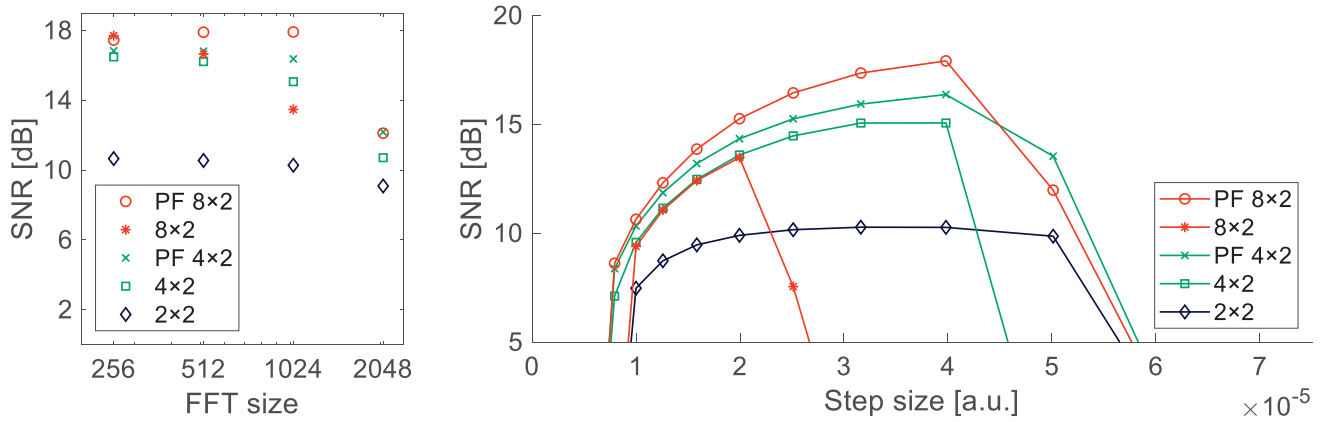


Fig. 7. Experimental results. (a) Maximum signal SNR after demodulation for each FFT size. (b) Relationship of step size and signal SNR.

A high-speed polarization scrambler (PS) and 10- and 40-m-long polarization maintaining fibers (PMF) were inserted into the system to determine if the MIMO AEQs could work under fast polarization fluctuations and PMD. We set the modulation speed of the PS at 11.01 Mrad/s. The signal light was amplified with two erbium-doped fiber amplifiers (EDFAs) placed after the transmitter and before the receiver. An optical band-pass filter (OBPF) cut amplified spontaneous emission noises outside the signal bandwidth and the receiver detected the signal mixed with a light from an LO using 100-GHz balanced photodetectors. Finally, the signal was demodulated by the receiver-side DSP. To emulate the IQ impairments in the transmitter and receiver, 3-ps IQ skews for X-polarization signals were imposed on the signals in the AWG and receiver-side DSP.

The receiver-side DSP followed the same process as in the simulation. We used (14) for the update in both PF 8×2 and 4×2 MIMO AEQs. We obtained H_T^l and H_R^l before the main measurement using 50-frame signals. We evaluated the SNR of ten consecutive frames and defined the SNR of the worst frames as that of the signal.

B. Results

We show the experimental results in Fig. 7. Fig. 7(a) shows the relationship between FFT size and SNR for each MIMO AEQ. The time window width (time width of the signals fed to the filters at a time) corresponding to each FFT size is also shown. Note that the step size is optimized by log-scale searching in 0.1-dB increments. Generally, a larger FFT size can improve the compensation accuracy by enabling compensation for spectrally fine impairments in the transmitter and receiver such as electrical signal reflections with large time delays, but it also reduces the tracking speed due to the larger interval between filter coefficient updates. As a result of the latter effect, the SNR decreased with the increasing FFT size with the conventional MIMO AEQ. In contrast, the PF 8×2 MIMO AEQ eased the trade-off and achieved the highest SNR among all configurations at an FFT size of 1024. For the 4×2 and 2×2 MIMO AEQ, the maximum SNR was worse than that of the 8×2 MIMO AEQs since the IQ impairments of either the transmitter or receiver or

both cannot be compensated. Note that no significant difference in the demodulated SNR was observed between the PF and conventional MIMO AEQs when polarization scrambling was not applied (e.g., the SNR was 21.9 and 21.8 for the PF and conventional 8×2 MIMO AEQ with an FFT size of 1024). Fig. 7(b) shows how the SNR changed when the FFT size was fixed at 1024 and the step size was varied. For each AEQ, the constellation of the frame with the best SNR is also shown. Comparing the conventional MIMO AEQ with the PF MIMO AEQ, we can see that, as in the simulation case, the lag-induced error decreased and the maximum step size increased. Especially in the PF 8×2 MIMO AEQ, the maximum step size can be nearly doubled and thus achieving an SNR improvement of 4.4 dB.

IV. CONCLUSION

In this article, we proposed PF MIMO AEQs as an approach to solve the problems of 4×2 and 8×2 MIMO AEQs: low SOP tracking speed and computational complexity. The proposed PF MIMO AEQs can reduce the total number of multiplexing in the filtering and updating operation to 1/2 or 3/4. We also show with numerical simulations and experiments that the PF MIMO AEQs can significantly improve the tracking speed to cope with 11 Mrad/s SOP fluctuation, which is beyond that caused by the electromagnetic effect via lightning strikes, the fastest natural source of SOP fluctuation. These indicate the PF MIMO AEQ is a promising technique for future high-information-rate optical receivers in practical applications.

APPENDIX A DERIVATION OF (4, 5)

This appendix explains a derivation of (4, 5). First, the inverse process of the signal transmission can be represented by cascaded multiplication of complex four-dimensional matrices and a vector:

$$\mathbf{s}_{in}^l(\omega) = H_T(\omega) H_{fiber}(\omega) H_R(\omega) \mathbf{s}_{out}(\omega) \quad (16)$$

Where

$$\mathbf{s}'_{in}(\omega) = \begin{pmatrix} s_{x,in}(\omega) \\ s_{x,in}^*(-\omega) \\ s_{y,in}(\omega) \\ s_{y,in}^*(-\omega) \end{pmatrix} \quad (17)$$

describes a four-dimensional input signal vector and $H_{fiber}(\omega)$ describes an inversed four-dimensional characteristic of optical effects within a fiber. Also, $H_R(\omega)$ and $H_T(\omega)$ describe the inversed electrical IQ impairment characteristic of the receiver and transmitter. For simplicity, the effect of the carrier frequency offset is omitted here. We put the elements of the $H_{SOP}(\omega)$ by

$$\begin{aligned} & H_{fiber}(\omega) \\ &= \begin{pmatrix} h_{CD}(\omega) & 0 & 0 & 0 \\ 0 & h_{CD}^*(-\omega) & 0 & 0 \\ 0 & 0 & h_{CD}(\omega) & 0 \\ 0 & 0 & 0 & h_{CD}^*(-\omega) \end{pmatrix} \\ &\times \begin{pmatrix} h_{xx}(\omega) & 0 & h_{xy}(\omega) & 0 \\ 0 & h_{xx}^*(-\omega) & 0 & h_{xy}^*(-\omega) \\ h_{yx}(\omega) & 0 & h_{yy}(\omega) & 0 \\ 0 & h_{yx}^*(-\omega) & 0 & h_{yy}^*(-\omega) \end{pmatrix} \quad (18) \end{aligned}$$

where the first matrix represents the inversed characteristics of CD and $h_{CD}(\omega)$ is an inversed CD characteristic. Also, the second represents inversed SOP-related effects of the transmission line including a combination of frequency-dependent SOP rotations, PMD, and PDL. It is a four-dimensional extension of the inversed Jones matrix made by combining the inversed two-dimensional Jones matrix with its complex conjugate. The elements $h_{xx}(\omega)$, $h_{xy}(\omega)$, $h_{yx}(\omega)$, $h_{yy}(\omega)$ defined here are equal to the same symbols in (6). We also put the elements of the $H_R(\omega)$ and $H_T(\omega)$ by

$$H_R(\omega) = \begin{pmatrix} 1 & h_{R11}(\omega) & 0 & h_{R12}(\omega) \\ h_{R11}^*(-\omega) & 1 & h_{R12}^*(-\omega) & 0 \\ 0 & h_{R21}(\omega) & 1 & h_{R22}(\omega) \\ h_{R21}^*(-\omega) & 0 & h_{R22}^*(-\omega) & 1 \end{pmatrix} \quad (19)$$

$$H_T(\omega) = \begin{pmatrix} 1 & h_{T11}^*(-\omega) & 0 & h_{T12}^*(-\omega) \\ h_{T11}(\omega) & 1 & h_{T12}(\omega) & 0 \\ 0 & h_{T21}^*(-\omega) & 1 & h_{T22}^*(-\omega) \\ h_{T21}(\omega) & 0 & h_{T22}(\omega) & 1 \end{pmatrix} \quad (20)$$

where we define (1, 2), (1, 4), (3, 2), (3, 4) elements of $H_R(\omega)$ by $h_{Rnm}(\omega)$ ($n, m = 1, 2$), and (2, 1), (2, 3), (4, 1), (4, 3) elements of $H_T(\omega)$ by $h_{Tnm}(\omega)$. Also, we put (1, 1), (3, 3) elements of these matrices as 1 and (1, 3), (3, 1) elements as 0, to fix redundant SOP-related DOFs. This is possible unless each frequency component of the signal becomes its complex conjugate due to large IQ impairments, such as IQ skew satisfying $\omega\tau = \pi$ (τ : IQ skew) for frequency ω . The other elements were determined automatically, since the elements in the even columns of the signal vector multiplied by $H_R(\omega)$ or $H_T(\omega)$ are always equal to the value obtained by taking the complex conjugate of the elements in the odd columns in the time domain.

Then, we split $H_{fiber}(\omega)$ to $H_{fiber}(\omega) = H_{fiber,1}(\omega) + H_{fiber,2}(\omega)$, where

$$H_{fiber,1}(\omega) = h_{CD}(\omega) \begin{pmatrix} h_{xx}(\omega) & 0 & h_{xy}(\omega) & 0 \\ 0 & 0 & 0 & 0 \\ h_{yx}(\omega) & 0 & h_{yy}(\omega) & 0 \\ 0 & 0 & 0 & 0 \end{pmatrix} \quad (21)$$

and

$$H_{fiber,2}(\omega) = h_{CD}^*(-\omega) \begin{pmatrix} 0 & 0 & 0 & 0 \\ 0 & h_{xx}^*(-\omega) & 0 & h_{xy}^*(-\omega) \\ 0 & 0 & 0 & 0 \\ 0 & h_{yx}^*(-\omega) & 0 & h_{yy}^*(-\omega) \end{pmatrix} \quad (22)$$

By using these matrices, we obtain

$$\begin{aligned} \mathbf{s}'_{in}(\omega) &= H_T(\omega) H_{fiber,1}(\omega) H_R(\omega) \mathbf{s}_{out}(\omega) \\ &+ H_T(\omega) H_{fiber,2}(\omega) H_R(\omega) \mathbf{s}_{out}(\omega) \quad (23) \end{aligned}$$

Then, by ignoring the even columns of $\mathbf{s}'_{in}(\omega)$ and calculating the matrix multiplication of each term, we can obtain

$$\begin{aligned} \mathbf{s}_{in}(\omega) &= H'_{SOP}(\omega) H'_R(\omega) h_{CD}(\omega) \mathbf{s}_{out}(\omega) \\ &+ H'^*_T(-\omega) H'^*_{SOP}(-\omega) H'^*_R(-\omega) h^*_{CD} \\ &(-\omega) \mathbf{s}_{out}(\omega) \quad (24) \end{aligned}$$

where $H'_{SOP}(\omega)$, $H'_R(\omega)$, $H'_T(\omega)$ are the matrices defined in (6)–(8). Finally, by comparing this equation to the equation of the conventional 8×2 MIMO AEQ without the carrier frequency offset

$$\begin{aligned} \mathbf{s}_{in}(\omega) &= H_{8 \times 2,1}(\omega) h_{CD}(\omega) \mathbf{s}_{out}(\omega) \\ &+ H_{8 \times 2,2}(\omega) Ph^*_{CD}(-\omega) \mathbf{s}_{out}(\omega) \quad (25) \end{aligned}$$

we obtain (4, 5).

REFERENCES

- [1] T. Kobayashi et al., "35-Tb/s C-band transmission over 800 km employing 1-Tb/s PS-64QAM signals enhanced by complex 8×2 MIMO equalizer," in *Proc. IEEE Opt. Fiber Commun. Conf. Exhib.*, 2019, Paper Th4B.2.
- [2] R. Rios-Müller, J. Renaudier, and G. Charlet, "Blind receiver skew compensation and estimation for long-haul non-dispersion managed systems using adaptive equalizer," *J. Lightw. Technol.*, vol. 33, no. 7, pp. 1315–1318, Apr. 2015.
- [3] C. R. S. Fludger and T. Kupfer, "Transmitter impairment mitigation and monitoring for high baud-rate, high order modulation systems," in *Proc. IEEE 42nd Eur. Conf. Opt. Commun.*, 2016, Paper Tu.2.A.2.
- [4] M. Arikawa and K. Hayashi, "Transmitter and receiver impairment monitoring using adaptive multi-layer linear and widely linear filter coefficients controlled by stochastic gradient descent," *Opt. Exp.*, vol. 29, pp. 11548–11561, Jul. 2021.
- [5] M. Sato, M. Arikawa, H. Noguchi, J. Matsui, J. Abe, and E. L. T. De Gabory, "Mitigation of transmitter impairment with 4×2 WL MIMO equalizer embedding preliminary CPR," in *Proc. IEEE Opt. Fiber Commun. Conf.*, 2022, Paper M1H.5.
- [6] X. Chen, J. Cho, A. Adamiecki, and P. Winzer, "16384-QAM transmission at 10 GBd over 25-km SSMF using polarization-multiplexed probabilistic constellation shaping," in *Proc. IEEE 45th Eur. Conf. Opt. Commun.*, 2019, Paper PD 3.3.
- [7] Z. Tao et al., "Characterization, measurement and specification of device imperfections in optical coherent transceivers," *J. Lightw. Technol.*, vol. 40, no. 10, pp. 3163–3172, May 2022.
- [8] P. S. R. Diniz, *Adaptive Filtering*, 4th ed. Berlin, Germany: Springer, 2012.
- [9] S. J. Savory, "Digital filters for coherent optical receivers," *Opt. Exp.*, vol. 16, pp. 804–817, Jan. 2008.

- [10] D. Charlton et al., "Field measurements of SOP transients in OPGW, with time and location correlation to lightning strikes," *Opt. Exp.*, vol. 25, pp. 9689–9696, Apr. 2017.
- [11] F. Pittalà, C. Stone, D. Clark, M. Kuschnerov, C. Xie, and A. Haddad, "Laboratory measurements of SOP transients due to lightning strikes on OPGW cables," in *Proc. IEEE Opt. Fiber Commun. Conf. Expo.*, 2018, Paper M4B.5.
- [12] J. J. Shynk, "Frequency-domain and multirate adaptive filtering," *IEEE Signal Process. Mag.*, vol. 9, no. 1, pp. 14–37, Jan. 1992.
- [13] M. Nakamura, T. Kobayashi, F. Hamaoka, and Y. Miyamoto, "High information rate of 128-GBaud 1.8-Tb/s and 64-GBaud 1.03-Tb/s signal generation and detection using frequency-domain 8×2 MIMO equalization," in *Proc. Opt. Fiber Commun. Conf. Exhib.*, 2022, Paper M3H.1.
- [14] M. Nakamura et al., "Over 2-Tb/s net bitrate single-carrier transmission based on >130 -GHz-bandwidth InP-DHBT baseband amplifier module," in *Proc. IEEE Eur. Conf. Exhib. Opt. Commun.*, 2022, Paper Th3C.1.
- [15] A. Kawai, M. Nakamura, M. Takahashi, T. Kobayashi, and Y. Miyamoto, "Partially frozen MIMO processing for fast polarisation tracking," in *Proc. IEEE Eur. Conf. Opt. Commun.*, 2022, Paper Th1C.2.
- [16] A. Kawai, M. Nakamura, T. Kobayashi, and Y. Miyamoto, "4-Dimensional IQ characteristic estimation for Polarization-multiplexed coherent transceivers," in *Proc. Opt. Fiber Commun. Conf.*, 2022, Paper M1H.2.
- [17] Q. Zhang et al., "Algorithms for blind separation and estimation of transmitter and receiver IQ imbalances," *J. Lightw. Technol.*, vol. 37, no. 10, pp. 2201–2208, May 2019.
- [18] T. Pfau, S. Hoffmann, and R. Noé, "Hardware-efficient coherent digital receiver concept with feedforward carrier recovery for M -QAM constellations," *J. Lightw. Technol.*, vol. 27, no. 8, pp. 989–999, Apr. 2009.
- [19] A. Matsushita, M. Nakamura, K. Horikoshi, S. Okamoto, F. Hamaoka, and Y. Kisaka, "64-GBd PDM-256QAM and 92-GBd PDM-64QAM signal generation using precise-digital-calibration aided by optical-equalization," in *Proc. Opt. Fiber Commun. Conf.*, 2019, Paper W4B.2.

Akira Kawai (Member, IEEE) received the B.S. and M.S. degree in physics from the University of Tokyo, Tokyo, Japan, in 2018 and 2020, respectively. In 2020, he joined the NTT Network Innovation Laboratories, Yokosuka, Japan. His research focuses on high-capacity optical transmission systems. He is a Member of the Institute of Electronics, Information and Communication Engineers of Japan.

Masanori Nakamura (Member, IEEE) received the B.S. and M.S. degrees in applied physics from Waseda University, Tokyo, Japan, in 2011 and 2013, respectively, and the Ph.D. degrees in electrical, electronic, and infocommunications engineering from Osaka University, Osaka, Japan, in 2021. In 2013, he joined NTT Network Innovation Laboratories, Yokosuka, Japan, where he engaged in research on high-capacity optical transport networks. He is a Member of the Institute of Electronics, Information, and Communication Engineers, Tokyo, Japan. He was the recipient of the 2016 IEICE Communications Society Optical Communication Systems Young Researchers Award.

Minami Takahashi received the B.S. degree in chemistry from Tohoku University, Sendai, Japan, in 2018, and the M.S. degree in chemistry from Nagoya University, Japan, in 2020. In 2020, she joined NTT Network Innovation Laboratories, Yokosuka, Japan. Her research interests include high-capacity optical transmission systems. She is a Member of the Institute of Electronics, Information, and Communication Engineers of Japan.

Takayuki Kobayashi (Member, IEEE) received the B.E., M.E., and Dr. Eng. degrees from Waseda University, Tokyo, Japan, in 2004, 2006, and 2019, respectively. In April 2006, he joined the NTT Network Innovation Laboratories, Yokosuka, Japan, where he was engaged in the research on high-speed and high-capacity digital coherent transmission systems. In April 2014, he moved to the NTT Access Network Service Systems Laboratories, Yokosuka, and was engaged in 5G mobile optical network systems. In July 2016, he moved back to the NTT Network Innovation Laboratories and has been working on high-capacity optical transmission systems. His research interests include long-haul optical transmission systems employing spectrally efficient modulation formats enhanced by digital and optical signal processing. He is a Member of the Institute of Electronics, Information and Communication Engineers of Japan. From 2016 to 2018, he was a Technical Program Committee Member of the Electrical Subsystems' Category for the Optical Fiber Communication Conference. Since 2018, he has been a TPC Member of the Point-to-Point Optical Transmission Category for the European Conference on Optical Communication.

Yutaka Miyamoto (Member, IEEE) received the B.E. and M.E. degrees in electrical engineering from Waseda University, Tokyo, Japan, in 1986 and 1988, respectively, and the Dr. Eng. degree in electrical engineering from Tokyo University, Tokyo, in 2016. In 1988, he joined NTT Transmission Systems Laboratories, Yokosuka, Japan, where he was engaged in the research and development of high-speed optical communications systems, including the 10-Gbit/s first terrestrial optical transmission system (FA-10G) using erbium-doped fiber amplifiers (EDFA) inline repeaters. From 1995 to 1997, he was with NTT Electronics Technology Corporation, Yokohama, Japan, where he was engaged in the planning and product development of high-speed optical module at the data rate of 10 Gb/s and beyond. Since 1997, he has been with NTT Network Innovation Laboratories, Yokosuka, where he has contributed to the research and development of optical transport technologies based on 40/100/400-Gbit/s channel and beyond. He is currently a NTT Fellow and the Director of the Innovative Photonic Network Research Center, NTT Network Innovation Laboratories, where he is investigating and promoting the future scalable optical transport network with the Pbit/s-class capacity based on innovative transport technologies, such as digital signal processing, space division multiplexing, and cutting-edge integrated devices for photonic preprocessing. He is a Fellow of the Institute of Electronics, Information, and Communication Engineers.